AIAA JOURNAL
Vol. 40, No. 10, October 2002

Computation of Subsonic Inviscid Flow past a Cone Using High-Order Schemes

Jae Wook Kim* and Philip J. Morris†
Pennsylvania State University, University Park, Pennsylvania 16802

A wake-dominated unsteady flow of Mach number 0.2 past a cone of vertex angle 60 deg is calculated numerically using high-order finite difference schemes on structured grids. The three-dimensional compressible Euler equations are solved to simulate an inviscid flow that exhibits large fluctuations of pressure and velocity as a result of the shedding of vortices behind the cone. An axisymmetric structured grid system is used. It is generated by rotating a two-dimensional grid plane around a centerline. The grid singularity at the centerline, where the Jacobian and some grid metrics approach infinity, is avoided by changing the form of the flux vectors in the Euler equations without any asymptotic assumption or simplification. Fourth- and sixth-order finite difference schemes are used for the evaluation of spatial derivatives, and a fourth-order Runge–Kutta scheme is used for marching the solution in time. The complex wake structures and motions behind the cone are investigated by visualizing the vorticity field. The mean flow pattern and periodic phenomena are analyzed and compared with experimental data. This demonstrates the accuracy of the present approach to further analyses of wake-dominated flows past axisymmetric blunt-based bodies.

I. Introduction

CALVERT[1] studied experimentally the low-speed flow patterns and the associated periodic phenomena of flow past cones with various vertex angles. He noted that there was little published work on incompressible flow past an axisymmetric blunt-based body, except some experiments carried out between the 1930s and 1960s. These earlier studies were restricted to flow visualization at low Reynolds numbers. He also discussed the periodic phenomena associated with such flows that are presumably related to some kind of regular vortex shedding: however, he noted that the actual wake pattern is unknown above a Reynolds number of a few hundred. Calvert's measurements of mean and fluctuating velocity and mean pressure for various cone angles show that the wakes for different cone vertex angles are all similar. This problem has received little attention in either experimental or computational studies during the last three decades. Recently, Long et al.[2] performed a simulation of a cone wake flow using low-order finite volume methods on unstructured grids. Souliez[3] extended these calculations to include a subgrid-scale turbulence model in a large eddy simulation (LES) of the cone flow. This gave an improved agreement with experiment. An understanding of the periodic wake phenomena in subsonic flow past blunt-based bodies is of importance in the design of airframe components such as landing gears, especially in relation to aerodynamic noise, but the existing knowledge of these flows is still far from complete. This paper seeks to provide some understanding of these complex flows through the simulation of the wake generated by an axisymmetric blunt-based cone.

The present paper focuses on the application of high-order finite difference schemes and structured grids to the computation of a three-dimensional, unsteady, inviscid, compressible flow past a cone at subsonic speeds. The scope of the present study is limited to the large scales of the wake turbulence and the shedding vortices, rather than the fine scales of turbulence whose simulation would demand huge computational resources and time. It is expected that essentially inviscid large-scale motions will dominate the turbulence in the separated wake flow and that viscous effects will be relatively unimportant. Therefore, the compressible Euler equations are used in the present computation, and the inviscid solution is provided as an asymptotic solution of the real viscous flow. Fourth- and sixth-order numerical schemes, based on central finite differences, are used for the solution of the Euler equations. These methods have been developed for high accuracy and high resolution in the direct computation of unsteady flows and acoustics.[4,5] In addition, an artificial dissipation model and time-dependent boundary conditions are combined with the high-order schemes for a long-time stable solution.[6–8]

The solutions are determined on a structured grid system generated by rotating a two-dimensional grid plane around the axis of symmetry. The axisymmetric structured grid has a grid singularity at the centerline, where the Jacobian and some grid metrics approach infinity. When a conventional form of the Euler equations is considered, this singularity makes it difficult to calculate the flux variables at the centerline and the flux derivatives near the centerline, when wide differencing stencils are used across the centerline in a generalized coordinate system. This paper proposes a way to avoid the centerline singularity by changing the form of the flux vectors in the Euler equations without any asymptotic assumption or simplification. In this way, all of the flux variables and derivatives can be evaluated without loss of accuracy. The singularity treatment is very useful in the calculation of the flux derivatives near the centerline; however, the Euler equations are still indeterminate at the centerline. In the present approach the solutions themselves at the centerline are interpolated from the neighboring values.

The problem conditions for the present computation are a freestream Mach number of 0.2 and cone vertex angle of 60 deg. The present work provides a visualization of the wake flowfield and its shed vortices and an analysis of the mean flow patterns and the periodic flow behavior. The results are compared with Calvert's experimental data[1] for validation of the solution, and the quantitative discrepancies between the inviscid and the viscous case are discussed. A spiral pattern of the wake flow behind the cone is shown clearly through a visualization of the wake vorticity field. The initial location of the regular vortex shedding and its Strouhal number are simulated correctly. These successful comparisons indicate that the present methodology is capable of describing three-dimensional, unsteady wake flows past axisymmetric blunt-based bodies.

In the next section the governing equations and the treatment of the centerline singularity are described. The high-order finite difference schemes are then introduced. The grid and initial and boundary

Received 1 August 2001; revision received 28 May 2002; accepted for publication 28 May 2002.

*Postdoctoral Research Associate, Department of Aerospace Engineering; currently BK21 Research Professor, Department of Aerospace Engineering, Korea Advanced Institute of Science and Technology, Daejeon 305-701, Republic of Korea.

†Boeing/A.D. Welliver Professor, Department of Aerospace Engineering. Associate Fellow AIAA.

conditions are then discussed. Both qualitative and quantitative results for the wake flowfield and a comparison with experiment are then presented.

II. Governing Equations and Centerline Singularity

The governing equations are the three-dimensional compressible Euler equations. The flux-vector form of the Euler equations, transformed to the computational domain, can be expressed in generalized coordinates as

$$\frac{\partial \hat{\boldsymbol{Q}}}{\partial t}+\frac{\partial \hat{\boldsymbol{E}}}{\partial \xi}+\frac{\partial \hat{\boldsymbol{F}}}{\partial \eta}+\frac{\partial \hat{\boldsymbol{G}}}{\partial \zeta}=\hat{\boldsymbol{0}} \tag{1}$$

where the flux vectors in generalized coordinates can be represented as

$$\begin{aligned}\hat{\boldsymbol{Q}}&=\boldsymbol{Q}/J, \qquad \hat{\boldsymbol{E}}=(1/J)(\xi_x\boldsymbol{E}+\xi_y\boldsymbol{F}+\xi_z\boldsymbol{G})\\ \hat{\boldsymbol{F}}&=(1/J)(\eta_x\boldsymbol{E}+\eta_y\boldsymbol{F}+\eta_z\boldsymbol{G})\\ \hat{\boldsymbol{G}}&=(1/J)(\zeta_x\boldsymbol{E}+\zeta_y\boldsymbol{F}+\zeta_z\boldsymbol{G})\end{aligned} \tag{2}$$

The conservative variables and the flux vectors in Cartesian coordinates are given by

$$\boldsymbol{Q}=\begin{bmatrix}\rho\\ \rho u\\ \rho v\\ \rho w\\ \rho e_t\end{bmatrix}, \qquad \boldsymbol{E}=\begin{bmatrix}\rho u\\ \rho u^2+p\\ \rho vu\\ \rho wu\\ (\rho e_t+p)u\end{bmatrix}$$

$$\boldsymbol{F}=\begin{bmatrix}\rho v\\ \rho uv\\ \rho v^2+p\\ \rho wv\\ (\rho e_t+p)v\end{bmatrix}, \qquad \boldsymbol{G}=\begin{bmatrix}\rho w\\ \rho uw\\ \rho vw\\ \rho w^2+p\\ (\rho e_t+p)w\end{bmatrix}$$

where the total energy per unit mass is defined as $e_t=p/[(\gamma-1)\rho]+(u^2+v^2+w^2)/2$ and $\gamma=c_p/c_v$ is the ratio of specific heats. $\gamma=1.4$ in the present computation. In Eq. (2) the transformation Jacobian J and the grid metrics $\xi_x,\ldots,\zeta_z$ are given by

$$J=1/[x_\xi(y_\eta z_\zeta-y_\zeta z_\eta)+x_\eta(y_\zeta z_\xi-y_\xi z_\zeta)+x_\zeta(y_\xi z_\eta-y_\eta z_\xi)] \tag{3}$$

with

$$\begin{bmatrix}\xi_x & \xi_y & \xi_z\\ \eta_x & \eta_y & \eta_z\\ \zeta_x & \zeta_y & \zeta_z\end{bmatrix}=J\begin{bmatrix}y_\eta z_\zeta-y_\zeta z_\eta & z_\eta x_\zeta-z_\zeta x_\eta & x_\eta y_\zeta-x_\zeta y_\eta\\ y_\zeta z_\xi-y_\xi z_\zeta & z_\zeta x_\xi-z_\xi x_\zeta & x_\zeta y_\xi-x_\xi y_\zeta\\ y_\xi z_\eta-y_\eta z_\xi & z_\xi x_\eta-z_\eta x_\xi & x_\xi y_\eta-x_\eta y_\xi\end{bmatrix} \tag{4}$$

In an axisymmetric structured grid the denominator in Eq. (3) becomes zero at the centerline, and the Jacobian approaches infinity. Therefore, all of the grid metrics expressed in Eq. (4) are indeterminate at the centerline. However, one can easily show that the ratios of the grid metrics to the Jacobian remain finite or zero at the centerline, even though the Jacobian and some grid metrics themselves have infinite values. This suggests a way to remove the centerline singularity. The key is to choose a different way of expressing the Jacobian and the grid metrics. New variables that replace the conventional Jacobian and the grid metrics are defined by

$$J^*\equiv 1/J=x_\xi(y_\eta z_\zeta-y_\zeta z_\eta)+x_\eta(y_\zeta z_\xi-y_\xi z_\zeta)+x_\zeta(y_\xi z_\eta-y_\eta z_\xi) \tag{5}$$

$$\begin{aligned}\begin{bmatrix}\xi_x^* & \xi_y^* & \xi_z^*\\ \eta_x^* & \eta_y^* & \eta_z^*\\ \zeta_x^* & \zeta_y^* & \zeta_z^*\end{bmatrix}&\equiv\frac{1}{J}\begin{bmatrix}\xi_x & \xi_y & \xi_z\\ \eta_x & \eta_y & \eta_z\\ \zeta_x & \zeta_y & \zeta_z\end{bmatrix}\\ &=\begin{bmatrix}y_\eta z_\zeta-y_\zeta z_\eta & z_\eta x_\zeta-z_\zeta x_\eta & x_\eta y_\zeta-x_\zeta y_\eta\\ y_\zeta z_\xi-y_\xi z_\zeta & z_\zeta x_\xi-z_\xi x_\zeta & x_\zeta y_\xi-x_\xi y_\zeta\\ y_\xi z_\eta-y_\eta z_\xi & z_\xi x_\eta-z_\eta x_\xi & x_\xi y_\eta-x_\eta y_\xi\end{bmatrix}\end{aligned} \tag{6}$$

The new variables with a superscript asterisk defined in Eqs. (5) and (6) have finite or zero values in the entire computational domain, including at the centerline. Using the new variables, the expressions for the flux vectors given by Eq. (2) become

$$\begin{aligned}\hat{\boldsymbol{Q}}&=J^*\boldsymbol{Q}, \qquad \hat{\boldsymbol{E}}=\xi_x^*\boldsymbol{E}+\xi_y^*\boldsymbol{F}+\xi_z^*\boldsymbol{G}\\ \hat{\boldsymbol{F}}&=\eta_x^*\boldsymbol{E}+\eta_y^*\boldsymbol{F}+\eta_z^*\boldsymbol{G}, \qquad \hat{\boldsymbol{G}}=\zeta_x^*\boldsymbol{E}+\zeta_y^*\boldsymbol{F}+\zeta_z^*\boldsymbol{G}\end{aligned} \tag{7}$$

In this manner the centerline singularity is removed, and all of the flux variables at the centerline can be evaluated. Especially, this treatment of the singularity benefits the calculation of the flux derivatives in Eq. (1) near the centerline when using wide differencing stencils across the centerline. However, the Euler equations still cannot be solved at the centerline itself, as J^* is zero there and the vector of the conservative variables $\hat{\boldsymbol{Q}}$ vanishes from Eq. (7). This means that Eq. (1) becomes indeterminate, and it is impossible to integrate the solutions in time. However, the solutions (conservative variables) at the centerline can be interpolated from the neighboring values.

III. High-Order Finite Difference Schemes

High-order finite difference schemes with high-resolution characteristics are used in the present computation on a structured grid. The main scheme is a pentadiagonal type of central compact finite difference scheme.[4,5] It is a generalization of the seven-point stencil Padé scheme used on the interior nodes. It can be expressed as

$$\beta f'_{i-2}+\alpha f'_{i-1}+f'_i+\alpha f'_{i+1}+\beta f'_{i+2}=\frac{1}{h}\sum_{m=1}^{3}a_m(f_{i+m}-f_{i-m}) \tag{8}$$

where f_i is an objective function for the flux variables and f'_i is its spatial derivative on the ith node. The grid spacing h is a constant independent of the index i in the computational domain where all of the grid points are equally spaced. Equation (8) can be solved by inverting a pentadiagonal matrix. The matrix must be completed at the boundaries. Therefore, noncentral or one-sided formulations other than Eq. (8) are needed on the boundary and the near-boundary nodes. These can be expressed as

$$f'_0+\alpha_{0,1}f'_1+\beta_{0,2}f'_2=\frac{1}{h}\sum_{\substack{m=0\\ m\neq 0}}^{3}a_{0,m}(f_m-f_0)$$

$$\text{for} \qquad i=0 \quad \text{(boundary node)} \tag{9}$$

$$\alpha_{1,0}f'_0+f'_1+\alpha_{1,2}f'_2+\beta_{1,3}f'_3=\frac{1}{h}\sum_{\substack{m=0\\ m\neq 1}}^{4}a_{1,m}(f_m-f_1)$$

$$\text{for} \qquad i=1 \tag{10}$$

$$\beta_{2,0}f'_0+\alpha_{2,1}f'_1+f'_2+\alpha_{2,3}f'_3+\beta_{2,4}f'_4=\frac{1}{h}\sum_{\substack{m=0\\ m\neq 2}}^{5}a_{2,m}(f_m-f_2)$$

$$\text{for} \qquad i=2 \tag{11}$$

The coefficients in Eqs. (8–11) are listed in Table 1. They are optimized, as described in Refs. 4 and 5, to achieve maximum resolution characteristics with fourth-order accuracy [second-order in Eq. (9) for numerical stability]. The optimized fourth-order compact finite difference schemes are used to evaluate the flux derivatives in the mean flow and radial directions. On the other hand, the flux derivatives in the azimuthal direction are calculated with a conventional central finite difference scheme for a simpler handling of the periodic condition across the branch cut. The standard central finite difference scheme is given by

$$f'_i=\frac{45(f_{i+1}-f_{i-1})-9(f_{i+2}-f_{i-2})+(f_{i+3}-f_{i-3})}{60h} \tag{12}$$

Table 1 List of optimized coefficients for compact finite difference schemes

Equation (8)	Equation (9)	Equation (10)	Equation (11)
$a_1 = 0.6511278808920836$	$a_{0,1} = -3.061503488555582$	$a_{1,0} = -0.5401943305881343$	$a_{2,0} = -0.1327404414078232$
$a_2 = 0.2487500014377899$	$a_{0,2} = 5.917946021057852$	$a_{1,2} = 0.8952361063034303$	$a_{2,1} = -0.6819452549637237$
$a_3 = 0.00614479661269978$	$a_{0,3} = 0.4176795271056629$	$a_{1,3} = 0.2553815577627246$	$a_{2,3} = 0.7109139355526556$
$\alpha = 0.5775233202590945$	$\alpha_{0,1} = 5.870156099940824$	$a_{1,4} = 0.007549029394582539$	$a_{2,4} = 0.2459462758541114$
$\beta = 0.08953895334666784$	$\beta_{0,2} = 3.157271034936285$	$\alpha_{1,0} = 0.1663921564068434$	$a_{2,5} = 0.003965415751510620$
——	——	$\alpha_{1,2} = 0.7162501763222718$	$\beta_{2,0} = 0.03447751898726934$
——	——	$\beta_{1,3} = 0.08619830787164529$	$\alpha_{2,1} = 0.4406854601950040$
——	——	——	$\alpha_{2,3} = 0.6055509079866320$
——	——	——	$\beta_{2,4} = 0.08141498512587530$

Equation (12) has sixth-order accuracy, which is the highest order of truncation for the given standard seven-point stencil. Combined with the high-order finite difference schemes in space, the classical fourth-order four-stage Runge–Kutta scheme is used for marching the solutions in time.

As mentioned in Sec. II, the solutions (conservative variables) are obtained at the centerline not by solving the governing equations but by interpolation from the neighboring solutions. In the present work a fourth-order interpolation is used at the centerline. It can be written as

$$f_0 = \frac{13(f_1 + f_{-1}) + 8(f_2 + f_{-2}) - 5(f_3 + f_{-3})}{32} \tag{13}$$

where the negative indexes mean the values in the opposite direction across the centerline. Actually, there are as many sets of the centerline solutions interpolated by Eq. (13) as half the number of grid points in the azimuthal direction. A unique value of the centerline solution is finally acquired by averaging these values.

High-order schemes in space and time resolve a wider range of wave number or frequency than low-order methods. However, even the present schemes do not resolve the highest wave-number or frequency range effectively; an adaptive nonlinear artificial dissipation model[7] is also used to remove the unwanted numerical oscillations that might develop from the unresolved range. The artificial dissipation model is implemented only at the last (fourth) stage of the Runge–Kutta scheme in order to minimize computational costs. In addition to the stringent requirements on the high-order and high-resolution numerical schemes, an accurate and robust calculation depends heavily on the suppression of any waves that might result from unwanted reflections on computational boundaries. The boundary conditions for a time-dependent problem should be physically correct and numerically well posed. Generalized characteristic boundary conditions[8] are used as the time-dependent boundary conditions in the present computation. Nonreflecting inflow/outflow and the inviscid wall conditions are imposed at the boundaries of the computational domain and the cone surface, respectively.

A validation of the accuracy of the high-order compact finite difference schemes, the adaptive nonlinear artificial dissipation model, and the generalized characteristic boundary conditions is described in Refs. 4–8. Multidimensional steady/unsteady and inviscid/viscous computations were considered in various benchmark problems: linear wave convection in Ref. 4, acoustic radiation from an axisymmetric baffle in Ref. 5, noise generation from airfoils in Ref. 6, shock-sound interaction in a transonic nozzle in Ref. 7, and wake flow and acoustic radiation from a circular cylinder in Ref. 8. It was shown that they produced very accurate numerical solutions in comparison with analytic solutions and experimental data. Thus they can be used effectively in the present computation.

IV. Procedure and Results of Numerical Simulation

In this section the numerical simulation of the unsteady inviscid compressible flow past a cone of vertex angle 60 deg in a subsonic stream of Mach number 0.2 is described. The simulation uses high-order finite difference schemes and the modified form of the flux vectors in the Euler equations in order to eliminate the centerline singularity.

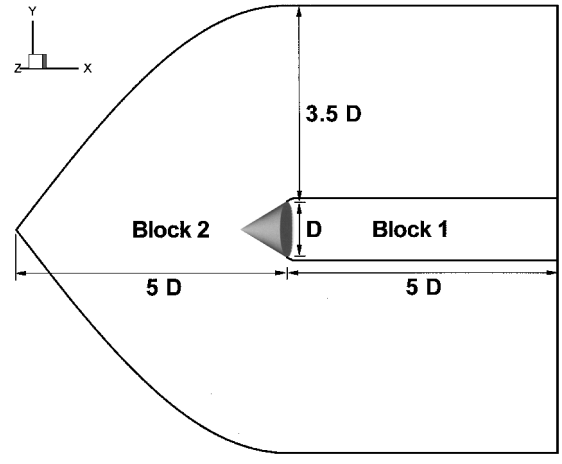

Fig. 1 Diagram of computational domain.

A. Grid System and Computation Procedure

For the present problem the computational domain consists of two blocks, and the rotation of a two-dimensional grid plane around the centerline as shown in Figs. 1 and 2 produces an axisymmetric grid system. The number of grid planes in the azimuthal direction is 48. The number of grid points is $101 \times 50 \times 48$ in block 1 and $161 \times 51 \times 48$ in block 2. This gives a total of 636,528 grid points. The grid points are clustered along the centerline and near the edge of the cone base. The minimum grid size at the center of the base is $\Delta x/D = 0.007$, $\Delta y/D = 0.007$, and $\Delta z/D = 2\pi \times 0.007/48$, where D is the base diameter.

The time step size is determined by the Courant–Friedrichs–Lewy condition,[9] which is given by

$$\Delta t = \min \frac{ChJ^*}{|U^*| + |V^*| + |W^*| + c\left(\sqrt{\xi_x^{*2} + \xi_y^{*2} + \xi_z^{*2}} + \sqrt{\eta_x^{*2} + \eta_y^{*2} + \eta_z^{*2}} + \sqrt{\zeta_x^{*2} + \zeta_y^{*2} + \zeta_z^{*2}}\right)} \tag{14}$$

with

$$U^* \equiv \xi_x^* u + \xi_y^* v + \xi_z^* w, \qquad V^* \equiv \eta_x^* u + \eta_y^* v + \eta_z^* w$$
$$W^* \equiv \zeta_x^* u + \zeta_y^* v + \zeta_z^* w$$

where the Courant number $C = 1.0$ is used in the present computation and c is the local speed of sound. In the evaluation of the time step, the operator min in Eq. (14) does not include the centerline as the denominator approaches infinity there, and the Euler equations are not solved on the centerline as remarked in the preceding sections.

A steady-state flowfield is first acquired by solving the two-dimensional axisymmetric Euler equations, not by the full

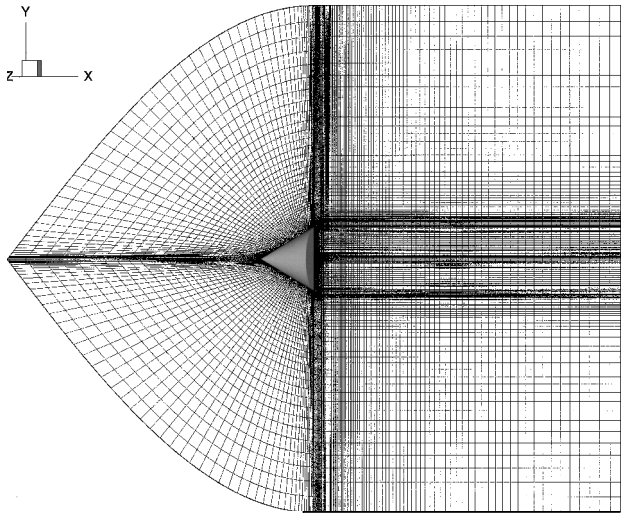

Entire view

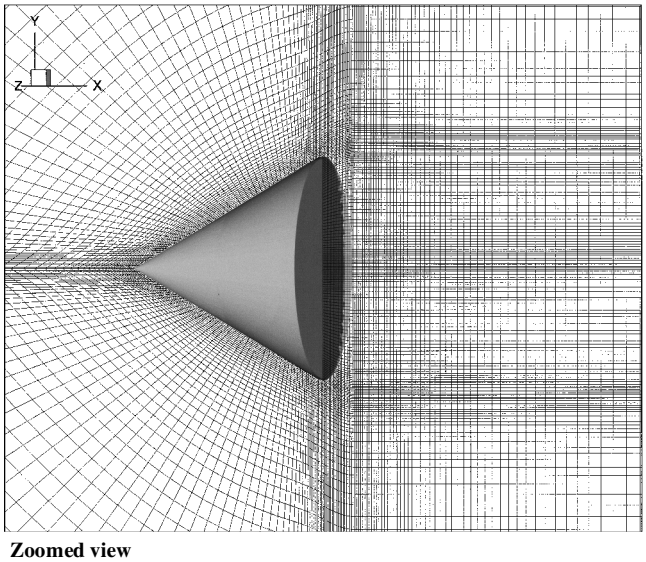

Zoomed view

Fig. 2 Grid mesh system.

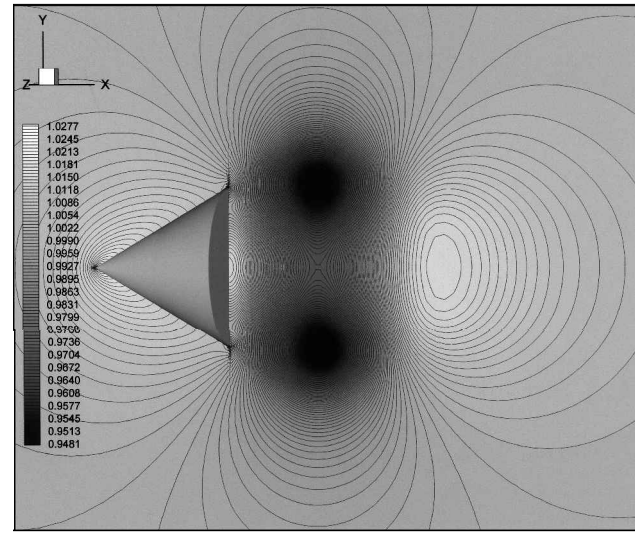

a) Pressure (p/p_∞)

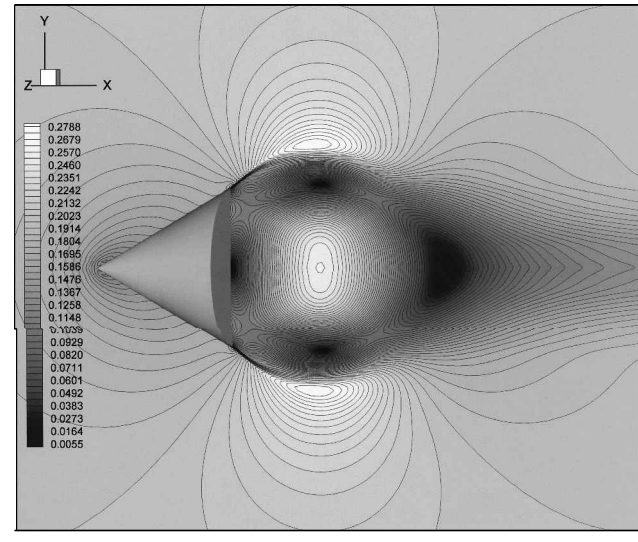

b) Mach-number contours

Fig. 3 Zoomed side view of axisymmetric steady-state flowfield for the initial condition.

three-dimensional equations. The three-dimensional initial flow field is constructed by rotation of the two-dimensional plane of the steady-state solution around the centerline. This is used as the initial condition for the present three-dimensional computation. Figure 3a shows the pressure contours, and Fig. 3b shows the Mach-number contours of the steady two-dimensional flow. There is a recirculation bubble in cone base region. Calvert[1] deduced this characteristic form from his experimental measurements. The calculation, using the OpenMP (data available on-line at http://www.openmp.org) parallel libraries, is performed on an IBM SP2 parallel computer at the Pennsylvania State University Center for Academic Computing (data available on-line at http://www.natasha.cac.psu.edu/beatnic/SPinfo/SP_features.php). Occupying four CPUs, the actual computation time is 4.45 s/iteration, which gives 7 μs/iteration/number of grid points. The computation performs 500,000 iterations in total: 200,000 iterations for a fully developed wake flow to be generated and 300,000 iterations for the mean flow patterns and the periodic flow behavior to be analyzed.

B. Initial Triggering of Vortex Shedding

In the early stages of the computation, it is difficult and time consuming to initiate vortex shedding in the inviscid flow without some excitation. To start the first vortex shedding, the velocity normal to the base of the cone is excited in the form

$$u_w(r,\theta,t) = \varepsilon u_\infty \sin^2(\pi r/R)\cos(2\theta)\exp\left[-(\ell n 2)(f_s t)^2\right]\sin(2\pi f_s t) \quad (0 \le r \le R, 0 \le \theta < 2\pi) \quad (15)$$

where ε is the amplitude of the fluctuation, u_∞ is the freestream velocity, r is the radial distance, R is the base radius, θ is the azimuthal angle, and f_s is the frequency of the excitation. In Eq. (15) the distribution of the excitation velocity has four lobes with alternating signs on the cone base, and the amplitude decreases rapidly to half its initial value in one time period. In the present computation the initial amplitude is chosen as $\varepsilon = 0.05$, and the frequency is $f_s = 0.171 u_\infty / D$. This corresponds to the regular vortex shedding frequency or the Strouhal number observed by Calvert.[1] Soon after the excitation vanishes, a nonaxisymmetric flowfield develops, and the first vortex shedding occurs.

C. Investigation of Flowfield

The unsteady wake flow might be visualized by the instantaneous pressure and Mach-number contours shown in Figs. 4 and 5 at the final time step. (Nondimensional time is $t^* = u_\infty t / D = 64.04$.) Figure 4 shows the longitudinal distribution in a side view, and Fig. 5 shows the circumferential distribution in a rear view. The instantaneous three-dimensional unsteady flowfield is very different from the two-dimensional axisymmetric steady flowfield shown in Fig. 2. The pressure contours show many irregular vortices generated from the edge of the cone base, and the Mach-number contours show strong flow fluctuations behind the cone base. The flow pattern appears to be random or chaotic, unlike the regular Kármán vortex street[10] behind a two-dimensional bluff body. It can be seen that

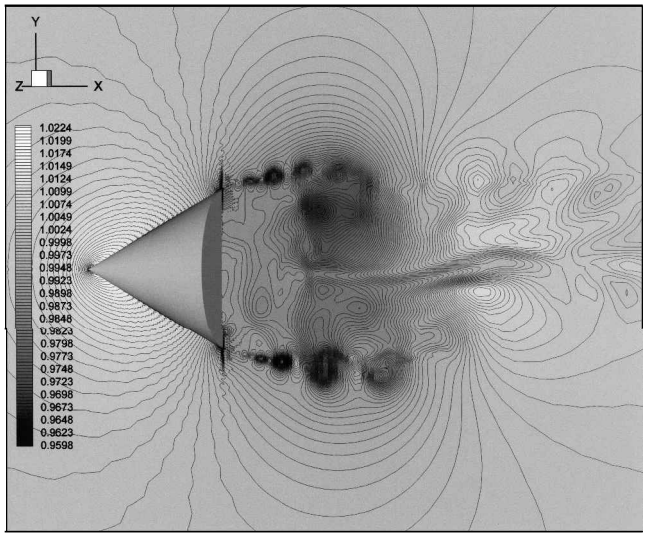

Pressure (p/p_∞)

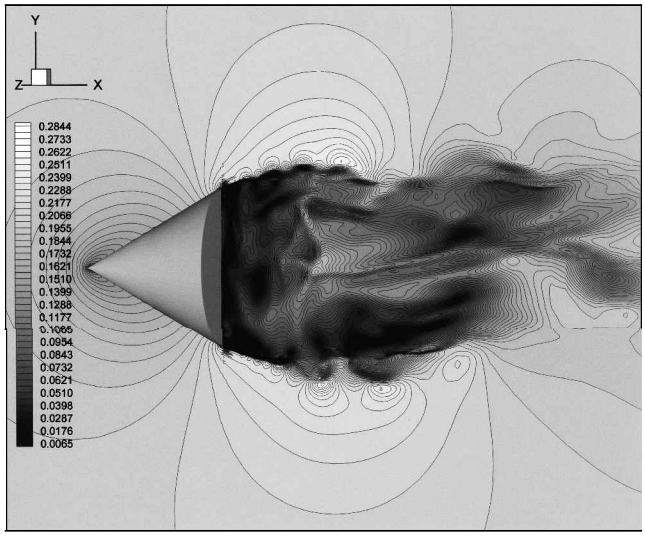

Mach-number contours

Fig. 4 Zoomed side view of instantaneous flowfield at the final time step.

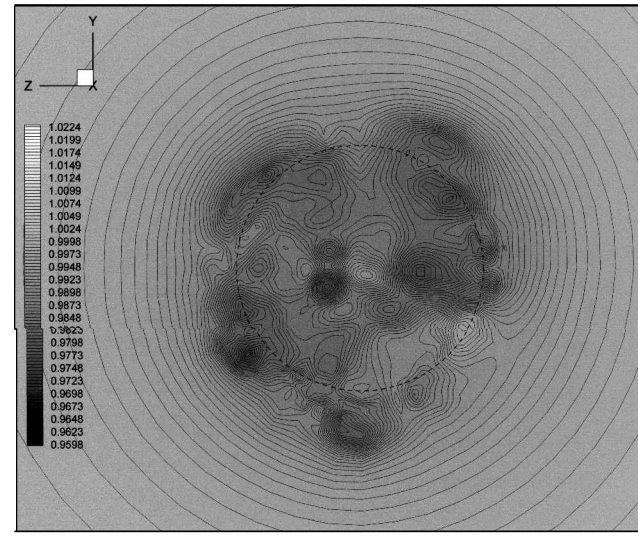

Pressure (p/p_∞)

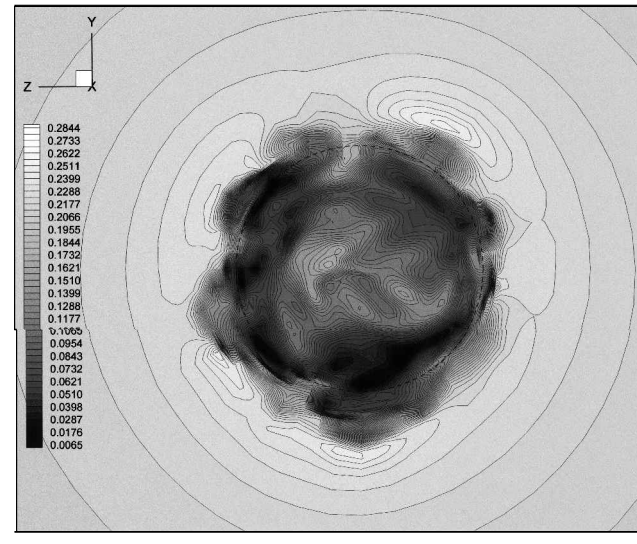

Mach-number contours

Fig. 5 Zoomed rear view of instantaneous flowfield at the final time step ($x/D = 1.0$ from the cone base).

some vortices pair and merge in the downstream region. This results in a large-scale motion of the far wake.

To examine the unsteady motion of the wake, time-traced snapshots of vorticity magnitude isosurfaces are presented in Fig. 6. Figure 6 shows some vortex rings near the cone base that have nonaxisymmetric distorted shapes, which induce chaotic flow fluctuations in the near wake and spontaneous vortex shedding downstream. It is also shown that the vortex rings in the near-wake region interact each other and change their shapes into axial vortex tubes in some transitional region away from the cone base at a distance nearly equal to the cone base diameter ($x/D \approx 1$). Farther downstream, the vortex tubes shed from the transitional region possess a velocity component in the circumferential direction. This results in a spiral motion of the far-wake structure. Moreover, the vortex tubes sometimes twist, bend, and stretch in the far-wake region. These phenomena occur quite randomly, and it is impossible to find any two snapshots with the same instantaneous flowfield during the entire computation. It is difficult to discern any periodicity from these time-traced observations of the flowfield. A frequency analysis of the flow signals is presented in a later section to quantify the periodicity.

D. Mean Flow Properties

The unsteady pressure and axial velocity along the centerline behind the cone are obtained as a function of time in the fully developed wake stage. By averaging the signals in time, the axial variations of the mean pressure and axial velocity can be obtained. They are compared with Calvert's experimental data[1] based on the Reynolds number of 5×10^4 in Figs. 7 and 8. Figure 7 shows that the mean pressure coefficient from the present computation agrees with the experimental data well in the near-wake region up to the location of its minimum value. It then recovers faster to the freestream value with a smaller overshoot than the experimental data in the far-wake region. Figure 8 shows that the mean velocity curve of the present computation is a little more positive than the experimental data and recovers slightly faster to the freestream value. The experimental points shown are based on the line through the data drawn by Calvert.[1] This avoids a jump in the velocity measurements near the stagnation point where the hot-wire measurement is inaccurate. The agreement between the predicted pressure coefficient and mean axial velocity is much better than that achieved in the low-order, unstructured grid calculations of Long et al.[2] However, the inclusion of a subgrid-scale turbulence model and a LES by Souliez[3] did improve the agreement with experiment. The mean stagnation point, where $\bar{u} = 0$ and $\overline{C_p} = 0$, of the present computation is slightly closer to the cone base than that of the experiment.

It is likely that the small discrepancy between the present results and the experimental data is caused by the difference between the inviscid flow and the real viscous flow. Usually, viscous vortex-boundary interactions dominate the flows around streamlined or slender bodies. In that case the shed vortices caused by the viscous separation are located within or very near the boundary layer. In

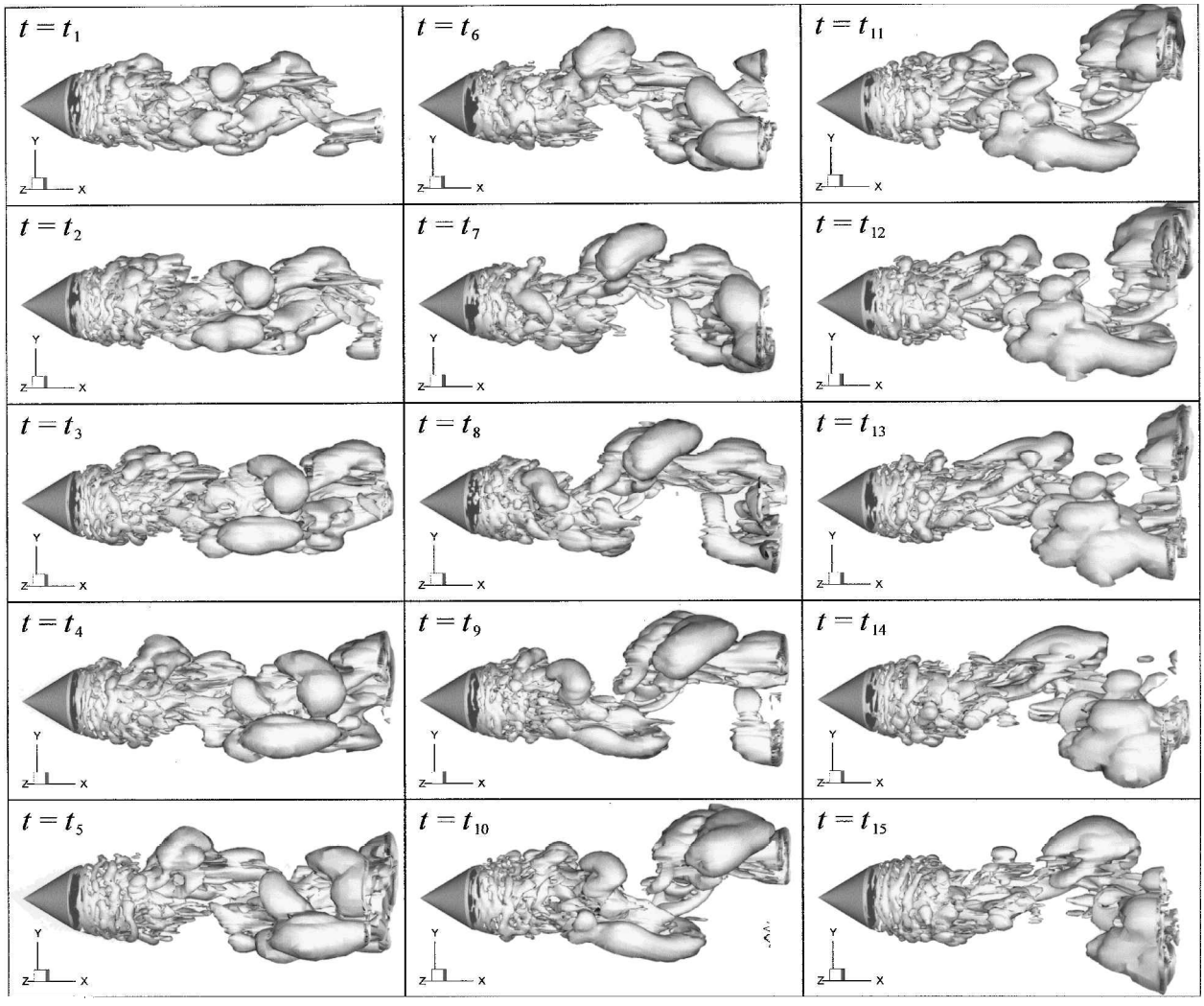

Fig. 6 Time-traced snapshots of vorticity magnitude isosurfaces (17 levels of $|\omega|D/u_\infty$ from 0.0 to 0.002) in the interval of time $t_{n+1} - t_n = 0.642D/u_\infty$ between two successive pictures.

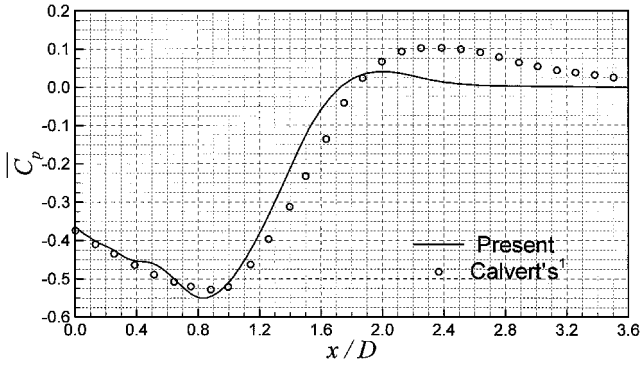

Fig. 7 Axial variation of mean pressure along the centerline behind the cone.

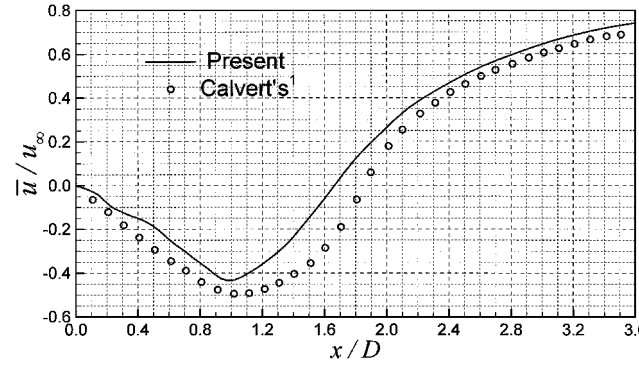

Fig. 8 Axial variation of mean axial velocity along the centerline behind the cone.

the present problem the viscous separation does not occur on the inclined surface of the cone but at the geometric separation at its sharp trailing edge. This shape of body was chosen for just this reason. The shed vortices are away from the attached boundary layers. From this point of view, we expect that viscous vortex-boundary interactions can be neglected. However, the Euler equations have no physical viscosity to dissipate kinetic energy of the flow as the wake moves downstream, which could be the reason for the fast recovery to the freestream value in the present case. The inviscid flow passes over a relatively smaller body in its effective size than the real viscous flow because there is no boundary-layer displacemens teffect. Also, it can be inferred that the core size of the vortices just near the cone edge is smaller and their strength is higher in the inviscid flow than in the real viscous flow. Therefore, the mean stagnation point is found to be closer to the cone base in the present case than in the experiment.

E. Flow Fluctuation Properties

Two variables are defined in Ref. 1 to characterize the fluctuating components of the flow. They are denoted by

$$\theta \equiv \frac{\overline{u'^2}^{\frac{1}{2}}}{u_\infty} \times 100, \qquad \phi \equiv \frac{\overline{u'^2}^{\frac{1}{2}}}{\bar{u}_m} \times 100$$

where $u' = u_m - \bar{u}_m$ is the fluctuation of the axial velocity about its mean value and $u_m = |u|$ is the magnitude of the axial velocity.

Table 2 Comparison of the results on various grid meshes for grid convergence test

Case	$\overline{C_p}=0$	$\overline{C_{p_{\min}}}$	$\overline{C_{p_{\max}}}$	fD/u_∞
Calvert's experiment[1]	$x/D=1.8$	$-0.53(x/D=0.9)$	$0.1(x/D=2.3)$	0.171
Grid 1 (101 pts.)	$x/D=1.73$	$-0.550(x/D=0.85)$	$0.040(x/D=2.02)$	0.171
Grid 2 (96 pts.)	$x/D=1.73$	$-0.548(x/D=0.85)$	$0.041(x/D=2.03)$	0.172
Grid 3 (91 pts.)	$x/D=1.74$	$-0.544(x/D=0.86)$	$0.045(x/D=2.05)$	0.169
Grid 4 (86 pts.)	$x/D=1.76$	$-0.539(x/D=0.87)$	$0.053(x/D=2.11)$	0.165

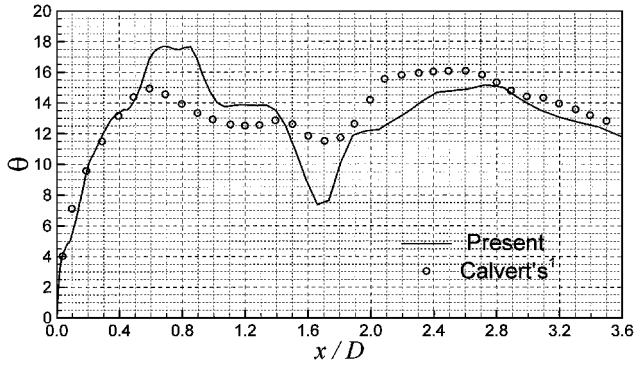

Fig. 9 Axial variation of velocity fluctuations in terms of freestream velocity.

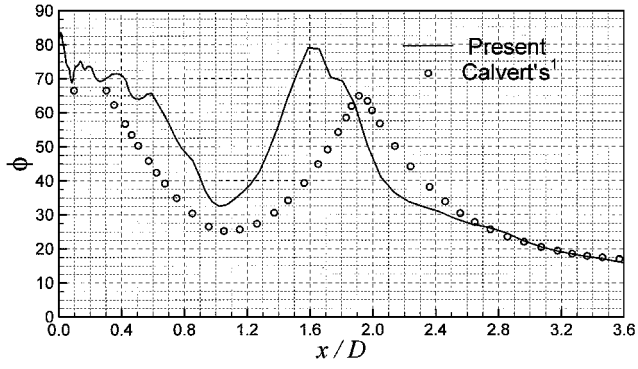

Fig. 10 Axial variation of velocity fluctuations in terms of the local axial velocity.

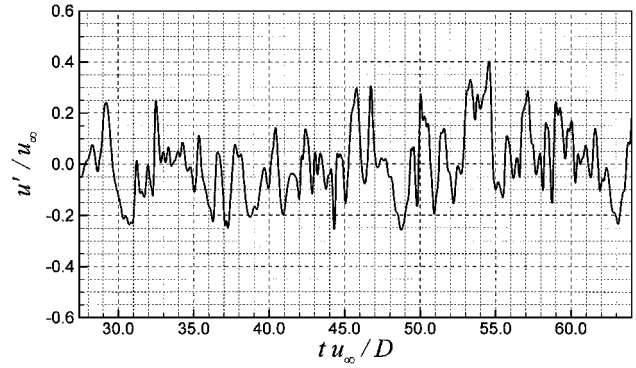

Time signal

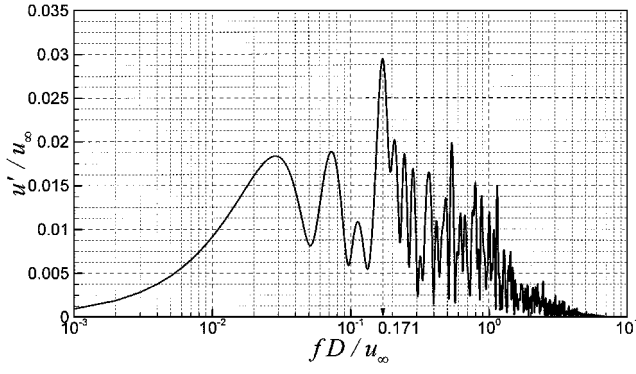

Frequency spectrum of the axial velocity fluctuations

Fig. 11 Periodicity of flow fluctuations at the point of mean pressure maximum.

Thus, θ is a measure of the absolute level of the velocity fluctuations, and ϕ represents the local turbulence intensity. The axial variations of θ and ϕ are shown and compared with the experimental data in Figs. 9 and 10, respectively. Figure 9 shows that the present results agree well overall with the experimental data except for a slight overshoot in the near-wake region and a small underprediction in the far-wake region. Figure 10 shows the same kind of discrepancy between the present results and the experimental data in terms of the shortening of the axial development as is explained for the mean flow results in Figs. 7 and 8. The predicted overall amplitude of the fluctuations agrees very well with the measurements. It is much closer to the experimental data than the predictions by Long et al.[2] particularly in the far-wake region. However, the present grid is much finer in that region, and the order of accuracy of the present numerical scheme is higher. A comparison of Figs. 8 and 10 shows that the region of the highest local turbulence intensities is in the vicinity of the stagnation point. This is consistent with Calvert's[1] observations. However, this high value is associated with the lower mean velocity at this location rather than an increase in the absolute value of the velocity fluctuations. In fact, as seen in Fig. 9, there is a slight decrease in the absolute value of the fluctuations in this region.

The point of the mean pressure minimum in Fig. 7 corresponds to the transitional region ($x/D \approx 1$), where the axial vortex tubes start to form as described in the preceding subsection. It coincides with the point of the mean velocity minimum where the highest speed of reversed flow on the centerline occurs as shown in Fig. 8. This point has significance in estimating the starting position of the periodic vortex shedding. Calvert[1] remarked that a periodic wake motion first appears in the region of the mean pressure minimum and that the periodicity presumably arises from the instability of the free shear layer in an adverse pressure gradient. He also mentioned that the periodicity is most prominent in the region of the mean pressure maximum. To quantify this periodicity, the frequency spectrum of the axial velocity is obtained at the point of the mean pressure maximum ($x/D = 2.0$). The time signal of the axial velocity fluctuations abstracted for the spectral analysis and its frequency spectrum at this point are shown in Fig. 11. The highest peak in Fig. 11 shows that there is a strong periodic wake motion at a nondimensional frequency of $fD/u_\infty = 0.171$. This is exactly the Strouhal number found by Calvert.[1] The existence of this peak is taken as further evidence that the present computation succeeds in simulating the dynamics of the vortex shedding process accurately.

F. Grid-Independence Study

In this section the grid convergence of the present computation is established to support the accuracy obtained in the preceding results and to show the robustness of the numerical algorithms and the boundary conditions used. The same computations have been carried out on three different numbers of grid points. The resolution is increased in the axial direction behind the cone with 96, 91, and 86 points. These are coarser than the original grid (101 points). The results of the grid-convergence test are given in Table 2, where the zero mean pressure point, mean pressure minimum, mean pressure maximum on the centerline, and Strouhal number are listed according to the four kinds of grid meshes. They are also compared with Calvert's experimental data. The grid-convergence test reveals that the result of the original computation has little grid dependency and the accuracy is verified.

V. Conclusions

The subsonic inviscid wake flow past a cone has been simulated using high-order finite difference schemes on structured grids. The present computation, performed in an axisymmetric structured grid system, is achieved by changing the form of the flux vectors in the Euler equations to remove the centerline singularity in the generalized coordinates. This approach makes it possible to investigate the complex wake flowfield and to obtain accurate values of the flow properties. It is shown that the vortex rings in the near wake change their shapes into axial vortex tubes in the far wake through a transitional region where periodic vortex shedding begins. A spiral motion of the wake is found. The mean flow pattern agrees well with the experimental data when account is taken of the likely differences between the inviscid and the viscous cases. It is confirmed that the point of the mean pressure minimum is the starting position of the periodic vortex shedding. A spectral analysis of this periodic phenomenon shows that its Strouhal number is 0.171. This is in exact agreement with the experimental observation. On the basis of the very good agreement between the predictions and experiment, it is proposed that the present methodology can be used for further analysis of wake-dominated flows past axisymmetric blunt-based bodies.

Acknowledgments

This research was supported by NASA Langley Research Center under Grant NRA 98-LaRC-5. The authors would like to acknowledge the Center for Academic Computing at Pennsylvania State University for providing the supercomputer resources.

References

[1]Calvert, J. R., "Experiments on the Low-Speed Flow past Cones," *Journal of Fluid Mechanics*, Vol. 27, No. 2, 1967, pp. 273–289.

[2]Long, L. N., Souliez, F. J., and Sharma, A., "Aerodynamic Noise Prediction Using Parallel Methods on Unstructured Grids," AIAA Paper 2001-2196, May 2001.

[3]Souliez, F. J., "Parallel Methods for Computing Unsteady Separated Flows Around Complex Geometries," Ph.D. Dissertation, Dept. of Aerospace Engineering, Pennsylvania State Univ., University Park, PA, Aug. 2002.

[4]Kim, J. W., and Lee, D. J., "Optimized Compact Finite Difference Schemes with Maximum Resolution," *AIAA Journal*, Vol. 34, No. 5, 1996, pp. 887–893.

[5]Kim, J. W., and Lee, D. J., "Implementation of Boundary Conditions for Optimized High-Order Compact Schemes," *Journal of Computational Acoustics*, Vol. 5, No. 2, 1997, pp. 177–191.

[6]Lockard, D. P., and Morris, P. J., "Radiated Noise from Airfoils in Realistic Mean Flows," *AIAA Journal*, Vol. 36, No. 6, 1998, pp. 907–914.

[7]Kim, J. W., and Lee, D. J., "Adaptive Nonlinear Artificial Dissipation Model for Computational Aeroacoustics," *AIAA Journal*, Vol. 39, No. 5, 2001, pp. 810–818.

[8]Kim, J. W., and Lee, D. J., "Generalized Characteristic Boundary Conditions for Computational Aeroacoustics," *AIAA Journal*, Vol. 38, No. 11, 2000, pp. 2040–2049.

[9]Hirsch, C., "The Von Neumann Method for Stability Analysis," *Numerical Computation of Internal and External Flows*, 1st ed., Vol. 1, Wiley, New York, 1992, pp. 283–341.

[10]Schlichting, H., "Outline of Boundary-Layer Theory," *Boundary Layer Theory*, 7th ed., McGraw–Hill, New York, 1979, pp. 24–46.

P. Givi
Associate Editor